1 Adaptive Optical Microscopy Using Image-Based Wavefront Sensing

Jacopo Antonello, Débora M. Andrade, and Martin J. Booth

1.1 Introduction

The most common approach to adaptive optics (AO), as originally employed in astronomical telescopes, has been to use a wavefront sensor to measure aberrations directly. In situations where such sensing provides reliable measurement, this is clearly the ideal method (see Chapter 2), but this approach has limitations, and particularly so in the context of microscopy. In order to understand this, one should consider the constraints the use of a wavefront sensor places on the nature of the optical configuration. A wavefront is only well defined in particular situations, for example, when light is emitted by a small or distant, pointlike object, such as a star for a telescope or a minuscule bead in a microscope. In these situations, a wavefront sensor provides a clear and reliable measurement, and this phenomenon has been used to great effect, as explained in Chapter 2. However, not all sources of light have these necessary properties. For example, a large, luminous object comprises an arrangement of individual emitters, each of which produces its associated wavefront. In this case, a wavefront sensor would respond to all of the light impinging upon it, thus giving potentially ambiguous measurements. In an extreme case, such as where light is emitted throughout the volume of the specimen, the sensor would be swamped with light and thus be unable to provide sensible aberration measurement. For this reason, in microscopy, direct wavefront sensing has been effective where pointlike sources have been employed, either through the introduction of fluorescent beads [1, 2] or using localized fluorescent markers [3] and nonlinear excited guide stars [4, 5, 6].

What happens if such sources cannot be employed? The use of beads or additional fluorescence markers in specimens is often not practical; nonlinear guide stars can only be produced in certain microscopes – particularly two-photon fluorescence microscopes – and require specialized and expensive laser sources. Moreover, all of these options are only relevant to fluorescence microscopes, but there are many other microscope modalities for which aberration correction might be required. A related challenge is that, if point sources cannot be used, then the source is by definition an extended object. How can one be certain that the aberration measured corresponds to that induced in the path to or from the focus, rather than to or from another region, perhaps out of focus or displaced laterally? A key observation is realizing that a microscope already has a method for determining the light that comes from the focal plane, as that is the light that forms the useful part of the image. The image itself can therefore be used indirectly as

the source for wavefront measurement, as long as the information contained within the image can be interpreted correctly.

The general approach to wavefront sensorless adaptive optics (or "sensorless AO" for short) relies upon the optimization of a measurement that is known to be related to the aberration content. For example, in an adaptive laser focusing system, one might maximize the intensity at the center of the focused beam. In image-based AO systems, which are a subcategory of sensorless AO systems, an appropriately chosen image property is optimized. In certain microscopes (e.g., confocal or multiphoton microscopes), the total image intensity (sum of all pixel values) is an appropriate optimization metric [7, 8, 9, 10, 11, 12, 13, 14, 15], as it exhibits a maximum value when no aberration is present. If the aberration in the system is nonzero due to refractive index variations in the specimen, then the value of the metric will be lower than its optimal value. The goal of the sensorless AO routine would be to use the adaptive element to maximize the metric by minimizing the total aberration in the system.

This concept can be illustrated through analogy with a user refocusing a microscope. The refocusing operation through translation of the specimen is optically equivalent to the application of a spherical phase aberration. The user has a good intrinsic appreciation of what constitutes an in-focus image, namely, that the features are sharp and the image shows the greatest amount of detail and contrast. If the object is not in focus, then the image appears blurred. The user changes the focus of the microscope until the quality of the image is maximized. Although this operation is performed subjectively, it is equivalent to a search algorithm, where the input variable (focal position) is changed until the quality metric (image sharpness or contrast, for example) is maximized.

A sensorless AO system is an extension of this concept, where the input variables correspond to all of the different aberration modes (e.g., spherical, coma, astigmatism) that can be corrected by the system and the image quality metric is defined mathematically, rather than subjectively. For practical operation, the algorithm used to find the optimal correction should be efficient, so that the number of measurements (and hence the time taken) is as small as possible.

There are other advantages to sensorless AO in microscopes. As the measurements are derived from images, the detected aberrations are certain to correspond to those that have affected the image formation. This is not necessarily the case when a wavefront sensor is employed, as different aberrations could affect the imaging and sensing optical paths, due to differences in their optical properties or to relative misalignment between the two paths. These errors in measuring the aberrations that affect the final image would not arise in the sensorless AO arrangement. In many practical systems, this can be an important consideration, as instrument aberrations can be appreciable. This is illustrated in Figure 1.1.

In principle, these sensorless AO schemes are broadly applicable across all microscopes, as there are relatively simple hardware and software requirements. On the hardware side, an adaptive element must be introduced into the microscope; on the software side, the only requirements are that a suitable combination of image quality metric and optimization procedure can be defined, in order to control the adaptive element. However, the wide range of microscope modalities means that each implementation
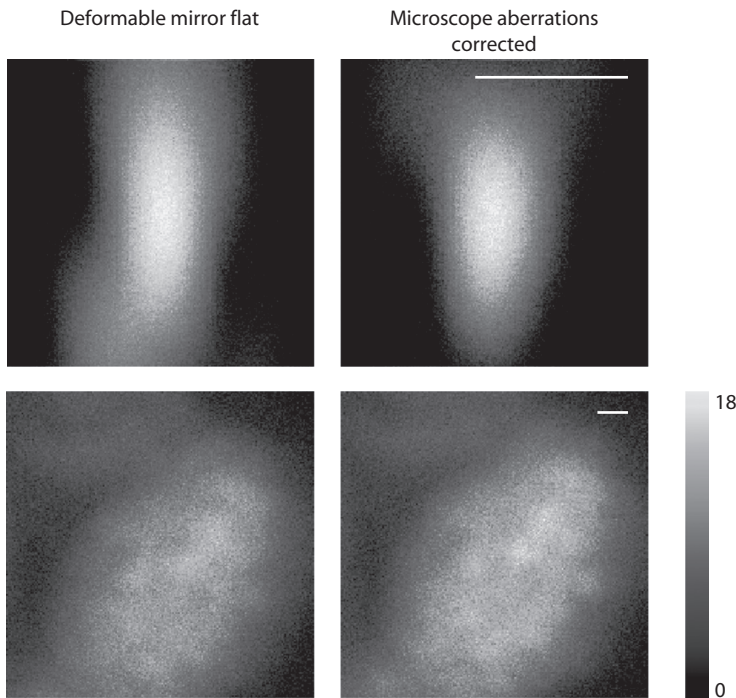
Figure 1.1 Correcting instrument aberrations with adaptive optics. (top) Axial sections of a confocal microscope PSF before (left) and after (right) correction of instrument aberrations. (bottom) Confocal image of a chloroplast located $30\,\mu m$ deep in intact plant tissue where instrument aberrations were not corrected (left) and where instrument aberrations were corrected (right). Even though specimen-induced aberrations were not yet compensated, there was a measurable improvement in the image after correction. Scale bars are $500\,nm$. Images are raw data.

will be different. Examples of a range of such implementations are shown in Figure 1.2. In this chapter, we elaborate on the principles behind the indirect, sensorless approach to wavefront measurement and outline the application of these schemes to a range of microscopes.

1.2 Simple Sensorless Adaptive Optics System

In order to explain the principles behind model-based AO systems, we use a simple optical system consisting of a focusing lens, an adaptive element, and a pinhole detector. While this system is not an imaging system – and hence cannot be used for image-based AO – it provides a useful basis for outlining the principles of sensorless aberration correction. The system, as illustrated in Figure 1.3, consists of an input beam whose wavefronts contain phase aberration $\Psi(r, \theta)$, which passes through an adaptive element that adds an aberration $\Phi(r, \theta)$. The beam is then focused by the lens onto a pinhole aperture placed before a photodetector. The pinhole diameter is chosen to be slightly
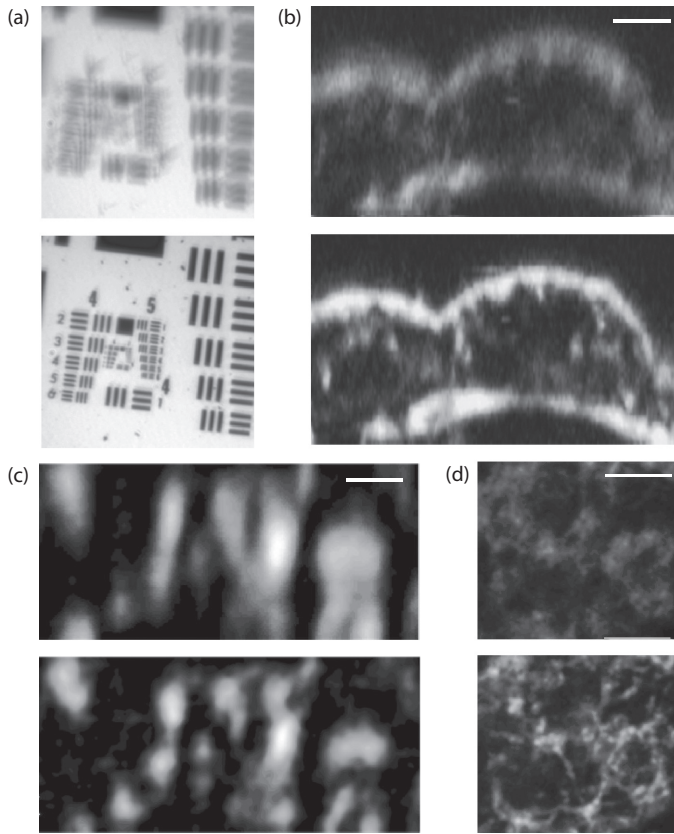
Figure 1.2 Correction results from image-based microscope AO systems, in each case showing images before and after aberration compensation. (**a**) Transmission microscope image of a US Air Force test chart. Reprinted with permission from [16], *Optics Express*. (**b**) Axial sections from third harmonic microscopy of mouse embryos; scale bar: 5 µm. Reprinted with permission from [12], *Optics Express*. (**c**) Axial sections from an AO 3D stimulated emission-depletion microscope (the precorrection image has been increased in brightness to highlight detail); scale bar: 1 µm. Reprinted with permission from [17], *Optics Express*. (**d**) Two-photon fluorescence images of neurons in a *Drosophila melanogaster* brain; scale bar: 5 µm. Images reproduced from references with the permission of the Optical Society (OSA).
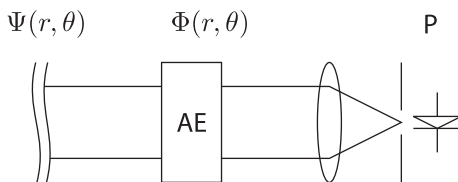
Figure 1.3 Simple optical system to illustrate the principles of sensorless adaptive optics. An input beam with phase aberration $\Psi(r, \theta)$ passes through an adaptive element (AE), which adds a phase aberration $\Phi(r, \theta)$, and is focused onto a photodetector covered by a pinhole (P).

smaller than the diffraction-limited spot, so that it samples the on-axis focal intensity. If the residual aberration $\Phi(r, \theta) + \Psi(r, \theta) = 0$, most of the light will pass through the pinhole and fall onto the photodetector. On the contrary, if the residual aberration is nonzero, a larger part of the light will be blocked by the pinhole, resulting in a lower signal being measured by the photodetector. In this simple situation, one can use the signal measured by the photodetector as a metric to apply aberration correction. In practice, to obtain aberration correction, one must sequentially apply different aberrations with the adaptive element and measure the corresponding value of the metric until this is maximized.

Frequently in AO, it is helpful to express aberrations using a modal expansion. The most common modal expansion uses Zernike polynomials [18] to describe aberrations, so that $\Phi(r, \theta)$ is expanded as follows:

$$\Phi(r, \theta) = \sum_{i=1}^{\infty} u_i \mathcal{Z}_i(r, \theta), \tag{1.1}$$

where u_i is the coefficient of the ith Zernike polynomial, $\mathcal{Z}_i$. Each coefficient u_i can be related to a geometrical aberration [19] such as defocus or astigmatism. In most practical situations, it is possible to represent significant aberrations with a small number of modes, so that the summation in Eq. (1.1) need only be taken over N terms. It is also sensible to neglect the first (piston) mode and assume $u_1 = 0$, as the piston mode constitutes the average value of the phase $\Phi(r, \theta)$, and it has no effect on the photodetector signal.

We consider the simple case of correcting 0.5 radians of defocus aberration $\mathcal{Z}_4$, so that we have $\Psi(r, \theta) = x_4 \mathcal{Z}_4(r, \theta)$, where $x_4 = 0.5$. A plot of the photodetector signal, which we use as our optimization metric m, is shown in Figure 1.4. It can be seen that m is a function of u_4, which is the amount of defocus that we introduce with the adaptive element. For $u_4 = -0.5$, the residual aberration $x_4 + u_4$ is zero, and the metric assumes the maximum value.

It is possible to treat the system in Figure 1.3 as a black box, where one can control u_4 and measure the corresponding value of the metric, but otherwise one has no further knowledge of the underlying system. In this scenario, one could apply a general optimization algorithm to maximize the metric. For example, in Figures 1.5 and 1.6, we applied, respectively, a genetic algorithm [20] and the Nelder–Mead algorithm [21]. The figures show the sequence of measurements required in each case to locate the maximum of the curve and the residual aberration at each stage of the process.

On the other hand, one can create a model for the system in Figure 1.3 that can be used to reduce the number of measurements that are necessary to maximize the metric. For example, when considering a vanishingly small pinhole, the metric signal measured with the photodetector corresponds to the intensity of the point-spread function measured at the origin of the image plane, I_0. From a classical result [22], it is known that for small aberrations, the Strehl ratio S, defined as the ratio between the aberrated and unaberrated focal intensities, is given by

$$S = \frac{I_0(x_4 + u_4)}{I_0(0)} \approx 1 - (x_4 + u_4)^2. \tag{1.2}$$
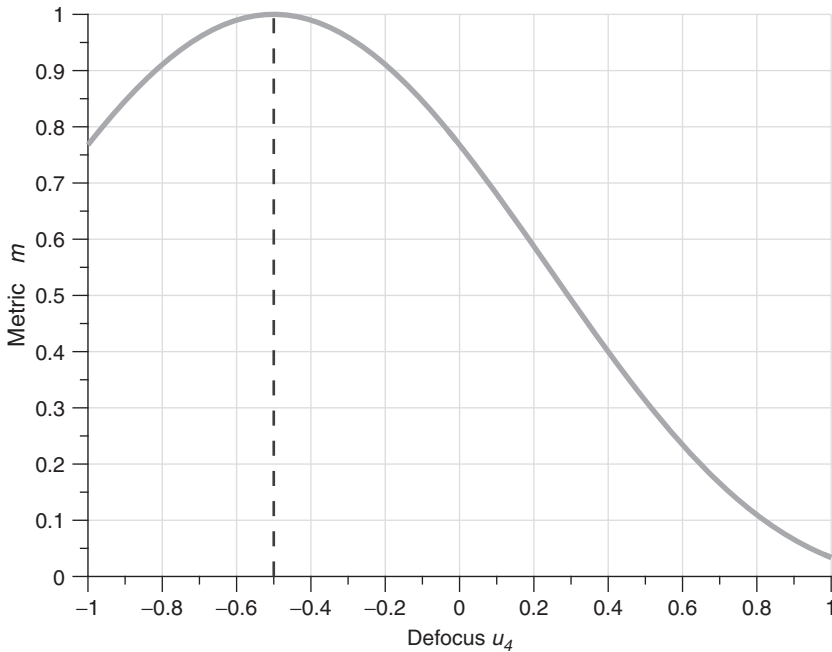
Figure 1.4 Plot of the optimization metric m (photodetector signal) as a function of applied correction aberration u_4. The metric has been normalized to its maximum value.

This suggests that one can model the metric in Figure 1.4 with a parabola, i.e., $m \approx I_0(0)(-u_4^2 + \alpha u_4 + \beta)$, where α and β are the coefficients of the parabola. By taking two measurements of the metric and solving a curve-fitting problem, one can estimate the coefficients α and β, which allows to determine the optimal value of u_4 that maximizes the metric. An example of applying this principle is depicted in Figure 1.7. As long as the initial aberration is in the region where the metric curve is approximately parabolic, the estimation of the aberration will be correct. It can be seen that this optimization method is more efficient than the previous black-box approach, where many more measurements were required.

If more aberration modes are present, as considered in Eq. (1.1), this procedure can be extended to include maximization of each mode. In this particular case, the mathematical principle is the same, but the parabola is replaced by a multivariate quadratic polynomial. An example comparison between the approach explained above and the Nelder–Mead algorithm is shown in Figure 1.8, where it can be seen that the former method is more efficient.

1.3   Image-Based Adaptive Optics Systems

An image-based AO system operates on many of the same sensorless AO principles outlined in the previous section. The main difference is that a single measurement now
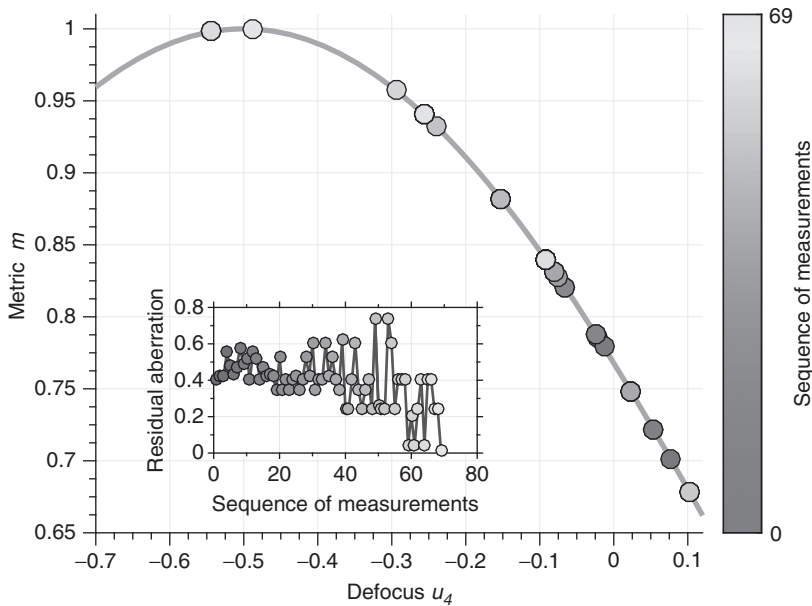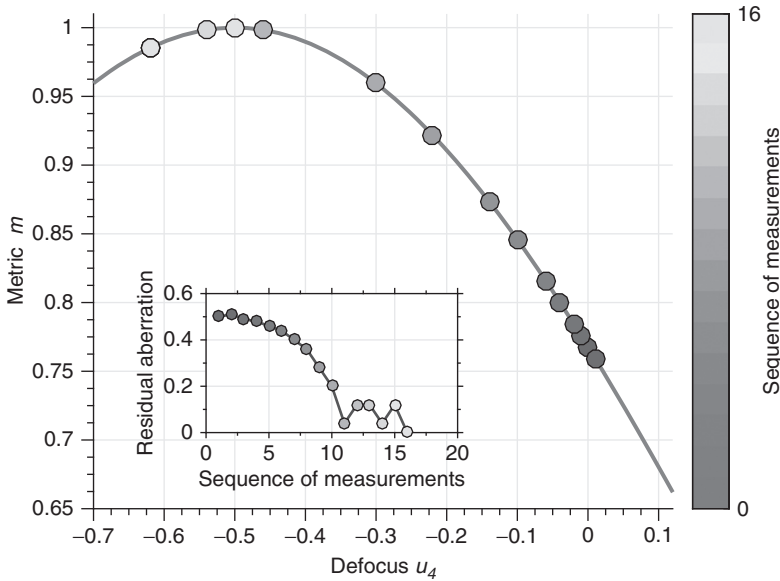
Figure 1.5 Optimization of the metric m using a genetic algorithm (GA). A GA is a search algorithm that tries to maximize a fitness function by simulating the process of natural selection. For the problem of aberration correction, the metric m is used as the fitness function. The population consists of a set of candidate values for u_4. For each member of the population, the GA measures the corresponding value of the metric m. The algorithm iteratively generates a new population by stochastically combining the members of the current population that exhibit a high fitness. This process results in a sequence of measurements of the metric m. Some values from such a sequence are plotted along the metric curve using a color map to indicate the order in which the measurements were acquired. The inset plot reports the residual aberration $|x_4 + u_4|$ for each measurement in the sequence.

involves acquiring a 2D image with a camera or recording a 2D image or a 3D volume when using a scanning microscope. The measurement obtained in this way is converted into a number using an image quality metric. One then optimizes the metric, as described in the previous section, using an appropriate optimization algorithm. In this section, we discuss additional aspects that should be considered when designing image-based AO systems.

1.3.1 Image Quality Metrics

Image quality is inherently a subjective measure that depends upon the type of microscope, the specimen, and the application. However, it is generally possible to define mathematically a metric that reflects the necessary properties that a user would attribute to a good image, i.e., an image obtained with zero aberration. For example, in a conventional wide-field microscope, an aberration-free image would have the sharpest features, so a measure of image sharpness or high spatial frequency content would be appropriate;

Figure 1.6 Optimization of the metric m using the Nelder–Mead (NM) algorithm. The NM is a search algorithm that repeatedly applies geometrical operations, such as reflection and expansion, to a simplex until it converges to the optimal value that maximizes m. In this particular case, with only one variable, the simplex consists of a line segment.
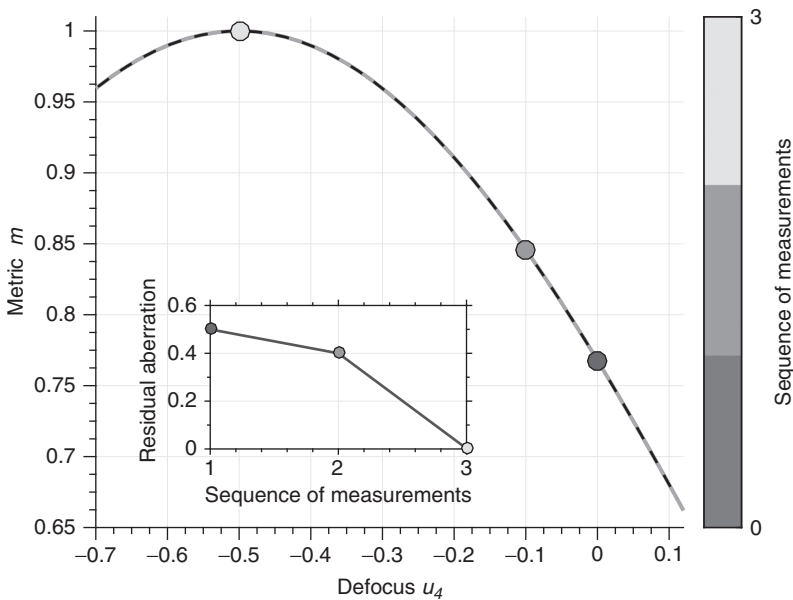
Figure 1.7 Optimization of the metric m by fitting a parabola through the sequence of measurements. The parabola is shown in the black dashed line and closely approximates the actual metric function.
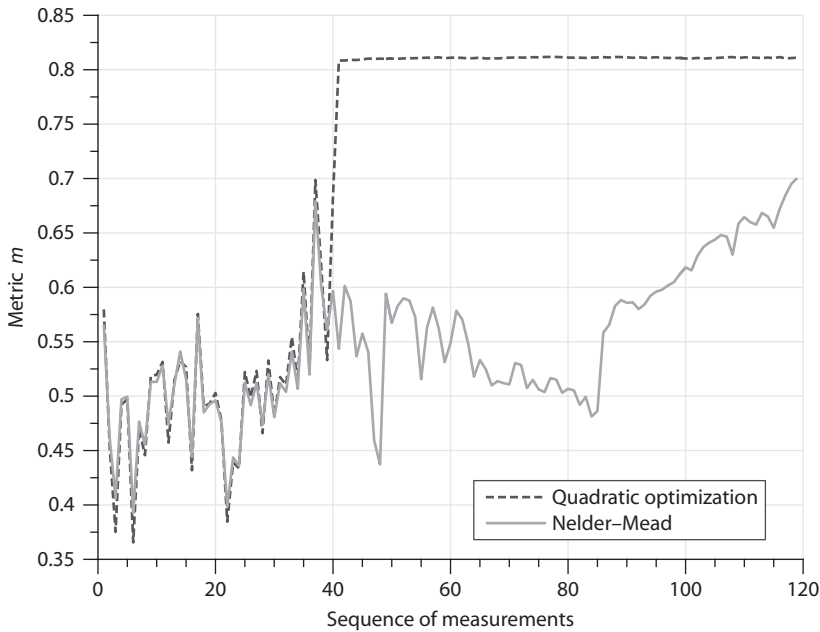
Figure 1.8 Example comparing one application of multivariate quadratic optimization algorithm [23] and the Nelder–Mead algorithm [21] using the same initial aberration for 37 aberration modes.

in a multiphoton microscope, the image brightness is strongly reduced by aberrations, so in this case, a metric based upon the sum of all pixel values (i.e., the total image intensity) would be relevant. In fact, multiple definitions of the image quality may be satisfactory for a given microscope type, which reflects the inherent subjectivity in assigning a numerical value to the quality of an image.

A suitable metric should satisfy some essential mathematical properties. In particular, it should ideally exhibit a global extremum (maximum or minimum) at which the residual aberration $x + u$ is zero by definition. The metric should not exhibit multiple local extrema close to the global extremum, as in such a case, apparently optimal solutions corresponding to nonzero residual aberration might be found. In this situation, the aberration correction problem would be mathematically ill posed and, in practice, prone to failure. As a final property, an ideal metric would resemble a convex or concave smooth function for a large range of values of the residual aberration, so that a simple optimization algorithm can be used to apply the aberration correction. Once we have defined the metric function, we can use knowledge of its properties and its dependence upon aberrations to design an estimation algorithm that provides efficient estimation of the required correction.
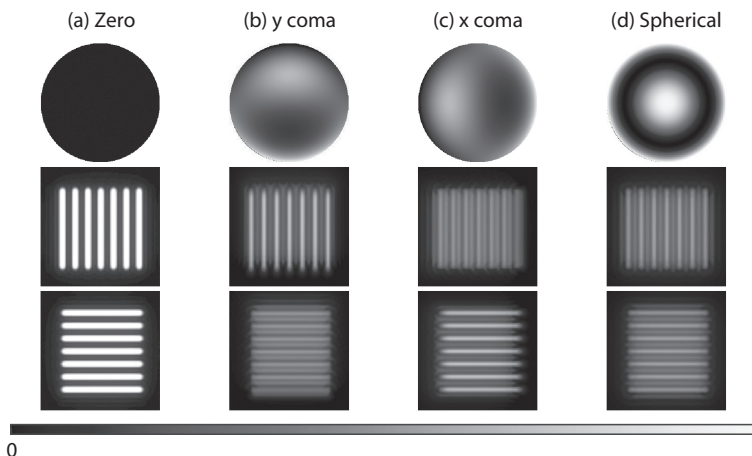
1.3.2 Effects of Specimen Structure

It is important to consider the intertwined effects of the specimen structure and aberrations on image formation. In many practical cases, an image can be expressed

by a convolution between a function representing the specimen structure, $f(\mathbf{p})$, and the point spread function (PSF) of the microscope, $h(\mathbf{p})$, where the vector $\mathbf{p}$ represents spatial position in three dimensions. In an incoherent imaging system, the image would therefore be expressed as

$$I(\mathbf{p}) = f(\mathbf{p}) \otimes h(\mathbf{p}) = \iiint f(\mathbf{p}' - \mathbf{p})h(\mathbf{p}') \, d\mathbf{p}'. \tag{1.3}$$

As a specific example, in a fluorescence microscope, f would represent the distribution of fluorescent markers, and h would be the intensity PSF of the microscope. It should be clear at this stage that the image I depends both on aberrations, via the PSF h, and on the specimen structure f. Ideally, an image-based AO scheme should be insensitive to specimen structure, providing the same aberration correction irrespective of the form of f. It is therefore important to take into account possible variation in specimen structure when designing the AO scheme. An illustrative example of such effects, comparing two different specimen structures, is found in Figure 1.9.

In certain situations, the specimen structure may have a particularly simple form. For example, if the specimen is a "guide star," as discussed in Chapter 2, one may replace f with the pointlike Dirac distribution, so that one is effectively measuring the PSF of the microscope. In such a case, the functional form of $I(\mathbf{p})$ is well known, and consequently, the functional form of the image quality metric can also be obtained. On the contrary, when f is given by a more involved function, or when one considers variations between specimens with significantly different structure, it is more challenging

Figure 1.9 Illustration showing how different aberrations affect the image quality when considering two specimen structures, each consisting of parallel lines in different orientations. Column (**a**) shows the images of the specimens when no aberration is present; column (**b**) shows the effect of y coma, column (**c**) the effect of x coma, and column (**d**) the effect of spherical aberration. The first row shows plots of the phase aberration function. Two specimens consisting of vertical lines (second row) and horizontal lines (third row) are shown using the same color map. Spherical aberration has a similar effect on the image quality of both specimens. On the contrary, y coma and x coma affect the image quality of the two specimens in different ways.

to predict the functional form of the image quality metric. This variability in the functional form affects the number of measurements that must be taken to unambiguously determine the correction aberration.

### 1.3.3   Effects of Different Aberration Modes

When one investigates the effects of aberrations on the image formation process of a microscope, it becomes apparent that different aberration modes affect images to differing degrees – the same magnitude of one mode can severely degrade the image, whereas another can have little or no effect. An obvious example of a mode that has no effect in most microscopes is piston (constant phase offset). Tip, tilt, and defocus modes, which collectively give rise to three-dimensional image displacements, could also be considered to have no effect on image quality, as they merely cause a translation in image position. It is usually sensible to remove such modes from the aberration correction procedure [14, 24], as they could produce undesirable image shifts, and applying them with the adaptive element may reduce the stroke that is available for correcting the other aberration modes that affect the image quality.

Some modes may be more dominant in a particular microscope due to the nature of the specimen – spherical aberration from a mismatch in refractive index is perhaps the most common example. In other cases, the image formation process of the microscope can enhance sensitivity to certain modes. This was revealed in structured illumination microscopy [25], where certain modes that affected the gridlike illumination pattern had greater effect than other modes. It was also seen that specimen-induced astigmatism could severely affect localization microscopes, which relied upon the same astigmatism mode to retrieve the axial position of emitters [26]. An example of the effect of incrementally correcting different aberrations modes is found in Figure 1.10.

1.3.4   Choice of Optimization Algorithm

The effectiveness of an image-based AO scheme depends greatly on the choice of optimization algorithm, alongside the modal representation (Section 1.2) and the definition of the image quality metric (Section 1.3.1). Image-based AO systems can in principle be built around any optimization algorithm, but considerable differences in performance can be observed between different approaches. We classify these algorithms into two different categories. The first class, which we refer to as model-free algorithms, comprises general optimization routines that were not specifically designed to tackle aberration correction problems. These algorithms make no assumption about the functional form of the image quality metric. The second class we denote as model-based algorithms. These methods assume that the image quality metric has a certain functional form, which constitutes the model.

Many different heuristic algorithms for model-free optimization have been developed [27]. Examples of such algorithms that have been applied in microscopy and imaging are hill-climbing algorithms [28, 29, 9, 30], evolutionary algorithms [7, 31, 9, 10, 11, 32], conjugate gradient methods [33], and stochastic parallel gradient descent
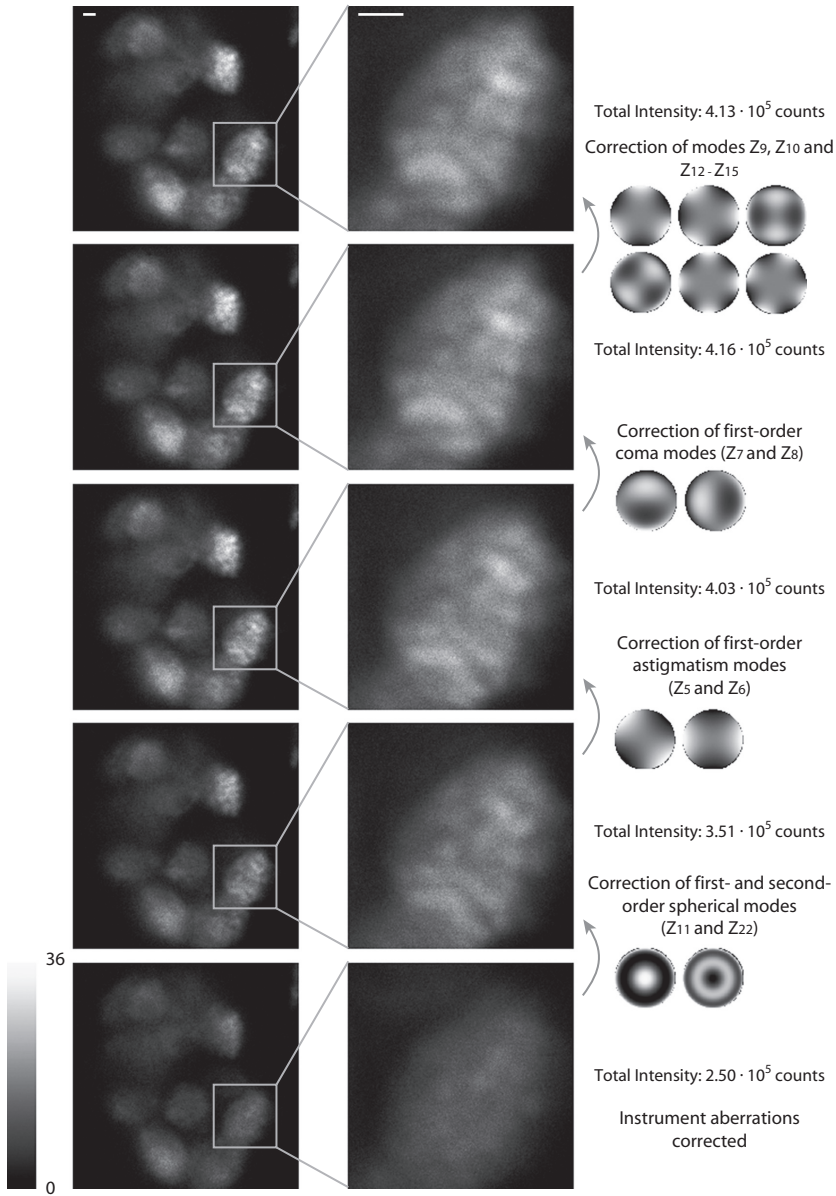
Figure 1.10 Chloroplasts in intact plant tissue imaged by confocal microscopy of endogenous fluorescence, 30 μm deep into the specimen. (bottom) When only instrument aberrations are corrected, imaging is still significantly precluded by specimen-induced aberrations. Image quality is gradually increased as the most severe aberrations are corrected, in this case, spherical aberrations, astigmatism, and coma. Typically, the improvement in image quality is very prominent for the first aberration modes corrected and stabilizes after a certain number of modes are corrected. The number of modes necessary to reach such a plateau depends on the specimen structure and possibly on the field of view. After aberration correction, the stacks of thylakoids within the chloroplasts, structures whose diameter ranges from approximately 300 to 500 nm, are clearly visible. Scale bars are 1 μm. The same linear color scale applies to all images. Images are raw data.

methods [34]. Such algorithms are designed to solve problems where very little background knowledge is available and where, contrary to the discussion in Section 1.3.1, the metric may have any functional form. For example, evolutionary algorithms, such as genetic algorithms, are typically used to tackle combinatorial problems, where differentiation cannot be applied, or strongly multimodal optimization problems [20]. As a result, these methods require a large number of measurements of the metric [35, 23, 36] and still may not converge to the global optimum [21]. In a sensorless AO system, this requires taking a large number of images before the aberration correction can be applied, which leads to long image acquisition times and increased specimen exposure. Overall, this means that model-free algorithms may be far from ideal in practical scenarios where one desires rapid measurement and low exposure.

In most microscopes, the effects of aberrations on the imaging process can be modeled using theory or measured through empirical observations. As such, an imaging model is usually available and can be used to inform the design of an efficient image-based AO scheme that should outperform any model-free approach. Image-based AO schemes built around such models have been implemented in a range of microscopes, including confocal [8], two-photon [37, 13, 14], harmonic-generation [12, 38, 24], wide-field [16], structured-illumination [25], stimulated emission depletion [39, 40, 17] (STED), and single-molecule localization microscopes [26]. In each case, an appropriate optimization metric had been defined that exhibited the desired properties outlined earlier. In several cases, such as confocal or multiphoton methods, the total image intensity was found to be appropriate, whereas other microscopes required more complex metric definitions, such as in the STED microscope, where a metric combining image brightness and sharpness provided the required properties.

Zernike polynomials often provide a convenient basis to concisely represent aberrations, as they include the three image displacement modes (tip, tilt, and defocus) and modes such as astigmatism, coma, and spherical aberration, which are frequently encountered in microscopy. Nevertheless, better performance might be achieved through use of modes derived from the mirror deformation functions [41]. The reason for this is that deformable mirrors can produce aberrations that are restricted by the mirror construction, for example, the arrangement of the actuators, and therefore can generate each Zernike mode with a varying degree of accuracy [42, 24]. It is, however, possible to derive [41] a set of mirror modes that exhibit the same orthogonality properties of Zernike modes but more closely represent the range of aberrations that the deformable mirror can generate. Generally, aberration correction has been applied considering around 10 to 20 low-order aberration modes, as this provided a sensible trade-off for most applications between the required capability of the active element and the expected benefit of the aberration correction [43]. See also Figure 1.10.

The optimization metric function has in different applications been approximated by quadratic [44, 35, 45, 16, 25, 13, 38, 46, 47, 14], Gaussian [25, 38], or Lorentzian functions [16, 13, 14]. Such functions provide an accurate model of the metric for aberrations within a certain range, which depends upon the type of microscope and the definition of the metric. In some cases, one may use multiple image quality metrics, for example, modeled by two different Gaussian functions. These can be used to handle

aberrations of different magnitudes, for example, by first correcting larger aberrations with a coarse accuracy and then correcting smaller aberrations with a finer accuracy [16].

The minimum number of measurements required to be able to compute a solution to the fitting problem depends on the number of free parameters of the function used to model the image quality metric. For instance, when considering Figure 1.7, the parabola has two unknown coefficients. The number of unknowns can reflect the variation that the metric exhibits for different specimen structures. For example, in sensorless adaptive optics systems where a final image is not formed [35, 48, 46, 23], the functional form of the metric is not affected by any specimen structure. In this case, correction of N aberration modes has been shown using as few as $N + 1$ measurements of the metric. On the contrary, for fully fledged imaging systems, such as [16, 25, 13, 38, 14, 15], aberration correction of N modes has been shown using at least $2N + 1$ measurements, as exemplified in Figure 1.11. In this case, the additional measurements are necessary to account for the interaction of the specimen structure with the PSF, as outlined in
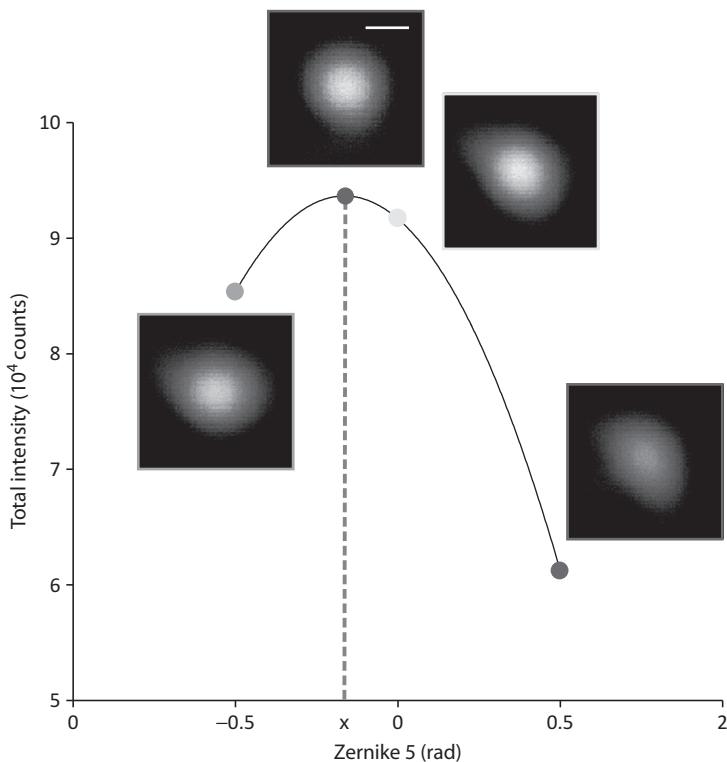
Figure 1.11 Basic principle of image-based adaptive optics. Here we exemplify the aberration correction procedure for the first-order astigmatism mode (Zernike 5) in a confocal microscope. By computing the total intensity of x-y images of a gold bead for symmetrical biases (± 0.5 rad rms) and for no bias, and fitting the plot with a parabola, the optimal bias may be determined as the coordinate of the peak of the parabola. This method is called the "$2N + 1$ algorithm" [25] because it requires a minimum of 2 times the number of modes to be corrected (symmetrical biases) plus 1 (0 bias) measurements. Scale bar is 200 nm and images are raw data.

(a)

(b)
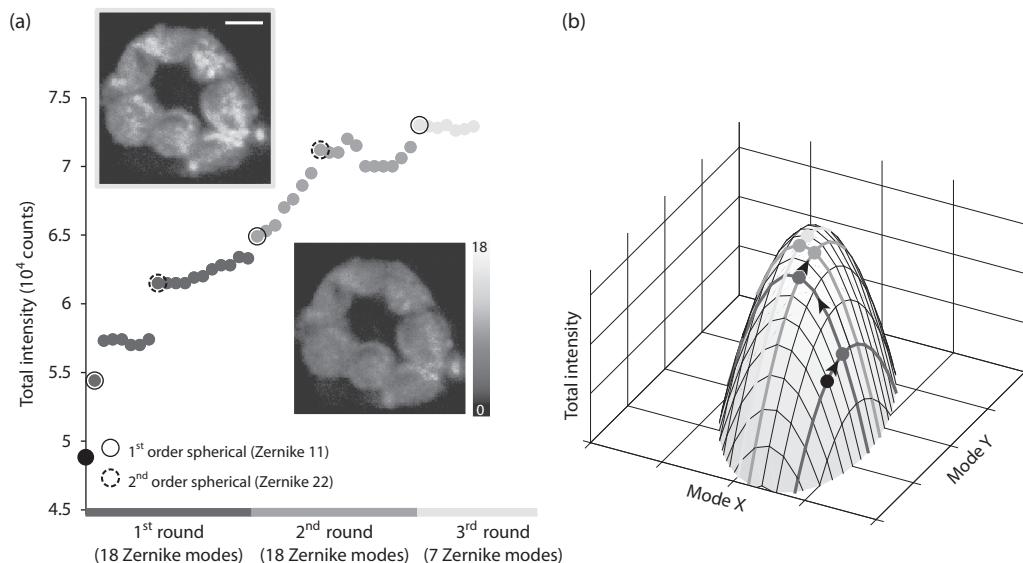
Figure 1.12 Convergence of optimization algorithm in sensorless adaptive optics. Here we show the variation in total intensity of an image (the adopted metric) throughout the optimization procedure. (**a**) Chloroplasts located $30\,\mu m$ deep in a broad bean plant leaf were imaged by confocal microscopy, and the improvement in the image quality metric can be seen as a function of individual Zernike modes corrected. In total, 18 Zernike modes were used, and the same correction procedure was repeated. The first- and second-order spherical modes were highlighted to exemplify the significant influence of these modes when imaging deep into tissue with prominent refractive index mismatch. The scale bar is $3\,\mu m$ and images are raw data. (**b**) Schematic illustrating why repetition of the aberration correction procedure may further improve image quality, for the simple case where only two aberration modes are present. The metric's dependence on the two orthogonal modes may be approximated by a paraboloid. If the main axes of such paraboloid are not aligned with the x and y axes [25], the convergence of the described optimization algorithm requires more than one round of correction [15]. In both (**a**) and (**b**), the black dot represents the initial state of the system. The first, second, and third rounds of corrections are indicated with the color map. More than one round of correction is required, as the axes of the paraboloid are not aligned with the coordinate axes. However, another set of modes can usually be chosen for which the axes are aligned [25], so that more efficient correction can be implemented. The image before the correction is reported in the inset with the color bar. The image after the correction is reported using the same color scale in the inset with the light border.

Eq. (1.3), which may result in detectable spatial variations in the functional form of the metric [24]. We further remark that collecting extra measurements in addition to the minimum necessary number improves the accuracy of the aberration correction [14]. Ultimately, factors such as the specific structure of the specimen, image noise, and the required level of correction will dictate how many measurements are required, especially if a mathematically optimum set of modes cannot be used, e.g., due to the limitations of the deformable mirror. Figure 1.12 demonstrates such a correction procedure in a confocal microscope using Zernike modes.

It should be noted that the speed of image-based aberration correction is limited only by the rate at which the necessary images can be acquired. As the metric is calculated from a whole image, useful measurements can be taken using images with far lower exposure levels that is usually required for the final scientific image. This means that the measurement images can be acquired much more quickly with fewer pixels and lower illumination levels than usually required for a good quality image. For example, measurement of $N = 10$ modes through a sequence of $2N + 1 = 21$ image acquisitions could be readily implemented in less than a second in a typical confocal microscope. As aberrations are predominantly static over an image period, the image-based AO method implemented in this way would be highly practical.

1.4   Conclusion

We have outlined in this chapter the principles behind adaptive optical microscopy through image-based aberration measurement. This approach has broad application across microscopy, although different schemes are required for each type of microscope. On the hardware side, it requires only the addition of an adaptive element into an existing microscope design. Once set up, image-based AO schemes are straightforward to operate and do not require complex computation. An image-based AO scheme requires specification of an image quality metric, a modal aberration expansion, and an optimization algorithm. While there are a wide range of model-free methods that can be used to optimize the metric, it is generally the case that model-based algorithms provide more efficient aberration correction, requiring a smaller number of images and hence less time and lower specimen exposure.

A drawback of current model-based algorithms is that they provide good correction only over a limited range of aberration amplitudes. However, this range can be extended through use of schemes that are sensitive over different aberration ranges. There is scope for further development of such schemes, for example, through the use of other optimization metrics and advanced optimization algorithms. Further advances could be made where spatial variations in aberrations are present. Current methods measure, in effect, an average of the aberrations across the image field, whereas it is known that significant variations may occur within this region [15, 49]. Image-based AO could be extended to measure these variations and be combined with multiconjugate AO correction to provide more accurate aberration compensation [50, 51].

In conclusion, we note that there are similarities between the concepts of sensorless AO explained in this chapter and the methods of scattering compensation described in Chapter 5 and subsequent chapters. In both cases, an image quality metric, such as total intensity, is optimized using a suitable algorithm. The main difference between these methods is the regime in which they operate: AO is concerned with compensation of low-order aberrations arising from the nonuniform refractive index distribution throughout relatively transparent specimens, whereas the methods of Chapter 5 and subsequent chapters are applicable to opaque, strongly scattering media, where multiple scattering events cause significant changes in amplitude and phase. Furthermore, in AO,

the expected performance of the corrected system would be equivalent to a Strehl ratio approaching the ideal value of 1; compensation of scattering, on the other hand, results in much lower Strehl ratios, although the improvement ratio after correction may be considerably higher than for AO systems.

1.5   References

[1] O. Azucena, J. Crest, J. Cao, W. Sullivan, P. Kner, D. Gavel, D. Dillon, S. Olivier, and J. Kubby, "Wavefront aberration measurements and corrections through thick tissue using fluorescent microsphere reference beacons," Opt. Express **18**, 17521–17532 (2010).

[2] X. Tao, Z. Dean, C. Chien, O. Azucena, D. Bodington, and J. Kubby, "Shack–Hartmann wavefront sensing using interferometric focusing of light onto guide-stars," Opt. Express **21**, 31282–31292 (2013).

[3] X. Tao, O. Azucena, M. Fu, Y. Zuo, D. C. Chen, and J. Kubby, "Adaptive optics microscopy with direct wavefront sensing using fluorescent protein guide stars," Opt. Lett. **36**, 3389–3391 (2011).

[4] X. Tao, A. Norton, M. Kissel, O. Azucena, and J. Kubby, "Adaptive optical two-photon microscopy using autofluorescent guide stars," Opt. Lett. **38**, 5075–5078 (2013).

[5] R. Aviles-Espinosa, J. Andilla, R. Porcar-Guezenec, O. E. Olarte, M. Nieto, X. Levecq, D. Artigas, and P. Loza-Alvarez, "Measurement and correction of *in vivo* sample aberrations employing a nonlinear guide-star in two-photon excited fluorescence microscopy," Biomed. Opt. Express **2**, 3135–3149 (2011).

[6] K. Wang, D. E. Milkie, A. Saxena, P. Engerer, T. Misgeld, M. E. Bronner, J. Mumm, and E. Betzig, "Rapid adaptive optical recovery of optimal resolution over large volumes," Nat. Methods **11**, 625–628 (2014).

[7] O. Albert, L. Sherman, G. Mourou, T. B. Norris, and G. Vdovin, "Smart microscope: an adaptive optics learning system for aberration correction in multiphoton confocal microscopy," Opt. Lett. **25**, 52–54 (2000).

[8] M. J. Booth, M. A. A. Neil, and T. Wilson, "New modal wave-front sensor: application to adaptive confocal fluorescence microscopy and two-photon excitation fluorescence microscopy," J. Opt. Soc. Am. A **19**, 2112–2120 (2002).

[9] A. J. Wright, D. Burns, B. A. Patterson, S. P. Poland, G. J. Valentine, and J. M. Girkin, "Exploration of the optimisation algorithms used in the implementation of adaptive optics in confocal and multiphoton microscopy," Microsc. Res. Techniq. **67**, 36–44 (2005).

[10] S. P. Poland, A. J. Wright, and J. M. Girkin, "Evaluation of fitness parameters used in an iterative approach to aberration correction in optical sectioning microscopy," Appl. Opt. **47**, 731–736 (2008).

[11] W. Lubeigt, S. P. Poland, G. J. Valentine, A. J. Wright, J. M. Girkin, and D. Burns, "Search-based active optic systems for aberration correction in time-independent applications," Appl. Opt. **49**, 307–314 (2010).

[12] A. Jesacher, A. Thayil, K. Grieve, D. Débarre, T. Watanabe, T. Wilson, S. Srinivas, and M. Booth, "Adaptive harmonic generation microscopy of mammalian embryos," Opt. Lett. **34**, 3154–3156 (2009).

[13] D. Débarre, E. J. Botcherby, T. Watanabe, S. Srinivas, M. J. Booth, and T. Wilson, "Image-based adaptive optics for two-photon microscopy," Opt. Lett. **34**, 2495–2497 (2009).

[14] A. Facomprez, E. Beaurepaire, and D. Débarre, "Accuracy of correction in modal sensorless adaptive optics," Opt. Express **20**, 2598–2612 (2012).

[15] J. Zeng, P. Mahou, M.-C. Schanne-Klein, E. Beaurepaire, and D. Débarre, "3D resolved mapping of optical aberrations in thick tissues," Biomed. Opt. Express **3**, 1898–1913 (2012).

[16] D. Débarre, M. J. Booth, and T. Wilson, "Image based adaptive optics through optimisation of low spatial frequencies," Opt. Express **15**, 8176–8190 (2007).

[17] B. R. Patton, D. Burke, D. Owald, T. J. Gould, J. Bewersdorf, and M. J. Booth, "Three-dimensional STED microscopy of aberrating tissue using dual adaptive optics," Opt. Express **24**, 8862–8876 (2016).

[18] F. Zernike, "Beugungstheorie des Schneidenverfahrens und seiner verbesserten Form, der Phasenkontrastmethode," Physica **1**, 689–704 (1934).

[19] V. N. Mahajan, "Aberrated point-spread functions for rotationally symmetric aberrations," Appl. Opt. **22**, 3035–3041 (1983).

[20] X. Yu and M. Gen, *Introduction to evolutionary algorithms* (Springer Science & Business Media, 2010).

[21] J. C. Lagarias, J. A. Reeds, M. H. Wright, and P. E. Wright, "Convergence properties of the Nelder–Mead simplex method in low dimensions," SIAM J. Optimiz. **9**, 112–147 (1998).

[22] M. Born and E. Wolf, *Principles of Optics*, 7th ed. (Cambridge University Press, 1999).

[23] J. Antonello, M. Verhaegen, R. Fraanje, T. van Werkhoven, H. C. Gerritsen, and C. U. Keller, "Semidefinite programming for model-based sensorless adaptive optics," J. Opt. Soc. Am. A **29**, 2428–2438 (2012).

[24] J. Antonello, T. van Werkhoven, M. Verhaegen, H. H. Truong, C. U. Keller, and H. C. Gerritsen, "Optimization-based wavefront sensorless adaptive optics for multiphoton microscopy," J. Opt. Soc. Am. A **31**, 1337–1347 (2014).

[25] D. Débarre, E. J. Botcherby, M. J. Booth, and T. Wilson, "Adaptive optics for structured illumination microscopy," Opt. Express **16**, 9290–9305 (2008).

[26] D. Burke, B. Patton, F. Huang, J. Bewersdorf, and M. J. Booth, "Adaptive optics correction of specimen-induced aberrations in single-molecule switching microscopy," Optica **2**, 177–185 (2015).

[27] Z. Michalewicz and D. B. Fogel, *How to solve it: modern heuristics* (Springer Science & Business Media, 2013).

[28] G. Vdovin, "Optimization-based operation of micromachined deformable mirrors," Proc. SPIE **3353**, 902–909 (1998).

[29] P. Marsh, D. Burns, and J. Girkin, "Practical implementation of adaptive optics in multiphoton microscopy," Opt. Express **11**, 1123–1130 (2003).

[30] L. P. Murray, J. C. Dainty, and E. Daly, "Wavefront correction through image sharpness maximisation," Proc. SPIE **5823**, 40–47 (2005).

[31] L. Sherman, J. Y. Ye, O. Albert, and T. B. Norris, "Adaptive correction of depth-induced aberrations in multiphoton scanning microscopy using a deformable mirror," J. Microsc. **206**, 65–71 (2002).

[32] K. F. Tehrani, J. Xu, Y. Zhang, P. Shen, and P. Kner, "Adaptive optics stochastic optical reconstruction microscopy (AO-STORM) using a genetic algorithm," Opt. Express **23**, 13677–13692 (2015).

[33] J. R. Fienup and J. J. Miller, "Aberration correction by maximizing generalized sharpness metrics," J. Opt. Soc. Am. A **20**, 609–620 (2003).

[34] M. A. Vorontsov, "Decoupled stochastic parallel gradient descent optimization for adaptive optics: integrated approach for wave-front sensor information fusion," J. Opt. Soc. Am. A **19**, 356–368 (2002).

[35] M. J. Booth, "Wave front sensor-less adaptive optics: a model-based approach using sphere packings," Opt. Express **14**, 1339–1352 (2006).

[36] A. J. Wright, S. P. Poland, J. M. Girkin, C. W. Freudiger, C. L. Evans, and X. S. Xie, "Adaptive optics for enhanced signal in CARS microscopy," Opt. Express **15**, 18209–18219 (2007).

[37] M. A. A. Neil, R. Juškaitis, M. J. Booth, T. Wilson, T. Tanaka, and S. Kawata, "Adaptive aberration correction in a two-photon microscope," J. Microsc. **200**, 105–108 (2000).

[38] N. Olivier, D. Débarre, and E. Beaurepaire, "Dynamic aberration correction for multiharmonic microscopy," Opt. Lett. **34**, 3145–3147 (2009).

[39] T. J. Gould, D. Burke, J. Bewersdorf, and M. J. Booth, "Adaptive optics enables 3D STED microscopy in aberrating specimens," Opt. Express **20**, 20998–21009 (2012).

[40] T. J. Gould, E. B. Kromann, D. Burke, M. J. Booth, and J. Bewersdorf, "Auto-aligning stimulated emission depletion microscope using adaptive optics," Opt. Lett. **38**, 1860–1862 (2013).

[41] M. Booth, T. Wilson, H.-B. Sun, T. Ota, and S. Kawata, "Methods for the characterization of deformable membrane mirrors," Appl. Opt. **44**, 5131–5139 (2005).

[42] G. Vdovin, O. Soloviev, A. Samokhin, and M. Loktev, "Correction of low order aberrations using continuous deformable mirrors," Opt. Express **16**, 2859–2866 (2008).

[43] M. Schwertner, M. Booth, and T. Wilson, "Characterizing specimen induced aberrations for high NA adaptive optical microscopy," Opt. Express **12**, 6540–6552 (2004).

[44] M. J. Booth, "Wavefront sensorless adaptive optics, modal wavefront sensing, and sphere packings," Proc. SPIE **5553**, 150–158 (2004).

[45] M. J. Booth, "Wavefront sensorless adaptive optics for large aberrations," Opt. Lett. **32**, 5–7 (2007).

[46] H. Linhai and C. Rao, "Wavefront sensorless adaptive optics: a general model-based approach," Opt. Express **19**, 371–379 (2011).

[47] D. Débarre, A. Facomprez, and E. Beaurepaire, "Assessing correction accuracy in image-based adaptive optics," Proc. SPIE **8253**, 82530F (2012).

[48] H. Song, R. Fraanje, G. Schitter, H. Kroese, G. Vdovin, and M. Verhaegen, "Model-based aberration correction in a closed-loop wavefront-sensor-less adaptive optics system," Opt. Express **18**, 24070–24084 (2010).

[49] M. J. Booth, "Adaptive optical microscopy: the ongoing quest for a perfect image," Light Sci. Appl. **3**, e165 (2014).

[50] R. D. Simmonds and M. J. Booth, "Modelling of multi-conjugate adaptive optics for spatially variant aberrations in microscopy," J. Opt. **15**, 094010 (2013).

[51] A. von Diezmann, M. Y. Lee, M. D. Lew, and W. E. Moerner, "Correcting field-dependent aberrations with nanoscale accuracy in three-dimensional single-molecule localization microscopy," Optica **2**, 985–993 (2015).